

# Short-Term Foreshoot and Aftershock Patterns of the 2021 $M_s$ 6.4 Yangbi Earthquake Sequence

Yingying Zhang<sup>1</sup>, Yanru An<sup>1,2</sup>, Feng Long<sup>3</sup>, Gaohua Zhu<sup>\*4</sup>, Min Qin<sup>5</sup>, Yusheng Zhong<sup>5</sup>, Qin Xu<sup>1</sup>, and Hongfeng Yang<sup>4</sup>

## Abstract

An  $M_s$  6.4 earthquake struck Yangbi County in western Yunnan province, China, on 21 May 2021, causing damage in the nearby region. Intensive foreshock activity started three days before the mainshock, and numerous aftershocks followed along a north-west-southeast-trending right-lateral main rupture fault. Double-difference relocation of the foreshock and aftershock sequence shortly before and after the  $M_s$  6.4 mainshock is conducted using the phase picks from the local seismic network. The focal mechanisms of relatively large foreshocks and aftershocks are also derived. The results not only delineate the ruptured fault geometry during the mainshock but also indicate the mechanism of static stress transfer according to the spatiotemporal evolution of foreshocks. The low background  $b$ -values around the mainshock are also consistent with the occurrence of the Yangbi earthquake sequence.

**Cite this article as** Zhang, Y., Y. An, F. Long, G. Zhu, M. Qin, Y. Zhong, Q. Xu, and H. Yang (2021). Short-Term Foreshoot and Aftershock Patterns of the 2021  $M_s$  6.4 Yangbi Earthquake Sequence, *Seismol. Res. Lett.* **93**, 21–32, doi: [10.1785/0220210154](https://doi.org/10.1785/0220210154).

## Supplemental Material

## Introduction

On 21 May 2021, an  $M_s$  6.4 earthquake struck Yangbi County in western Yunnan province, China, at the Beijing Standard Time of 21:48 (2021/05/21 13:48 UTC). This is the strongest earthquake in Yunnan since the 2014  $M_s$  6.6 Jinggu earthquake (Wang *et al.*, 2018) and has caused severe damage. As of 6 a.m. on 22 May, the earthquake has been reported to have caused 3 deaths and 27 injuries, leading to an estimated economic loss of 310 million CNY (48 million US\$). Focal mechanism solutions of the mainshock and network locations of early aftershocks show a strike-slip faulting mechanism of the mainshock, orienting southeast, parallel to the mapped Weixi-Qiaohou-Weishan (WQW) fault (Lei *et al.*, 2021; Long *et al.*, 2021; Su *et al.*, 2021; Yang, Liu, *et al.*, 2021; Zhang *et al.*, 2021). However, the locations of the 2021 Yangbi earthquake sequence are offset at least 15 km northwest of the mapped fault segment (Fig. 1b), posing the question of which fault was responsible for this earthquake. Furthermore, moderate-size earthquakes ( $M_s > 5.0$ ) had occurred northwest of the mainshock in 2013 and 2017 (Fig. 1b), following a trend parallel to the WQW fault. It is intriguing to derive characteristics of background seismicity to better understand the tectonophysics of these earthquakes and assess the potential seismic hazard.

The  $M_s$  6.4 Yangbi earthquake was preceded by numerous foreshocks starting from January 2021, including a few earthquakes with magnitudes larger than 3 (Fig. 2a) according to the catalog from China Earthquake Networks Center (CENC). It is worth noting that seismicity started to increase significantly

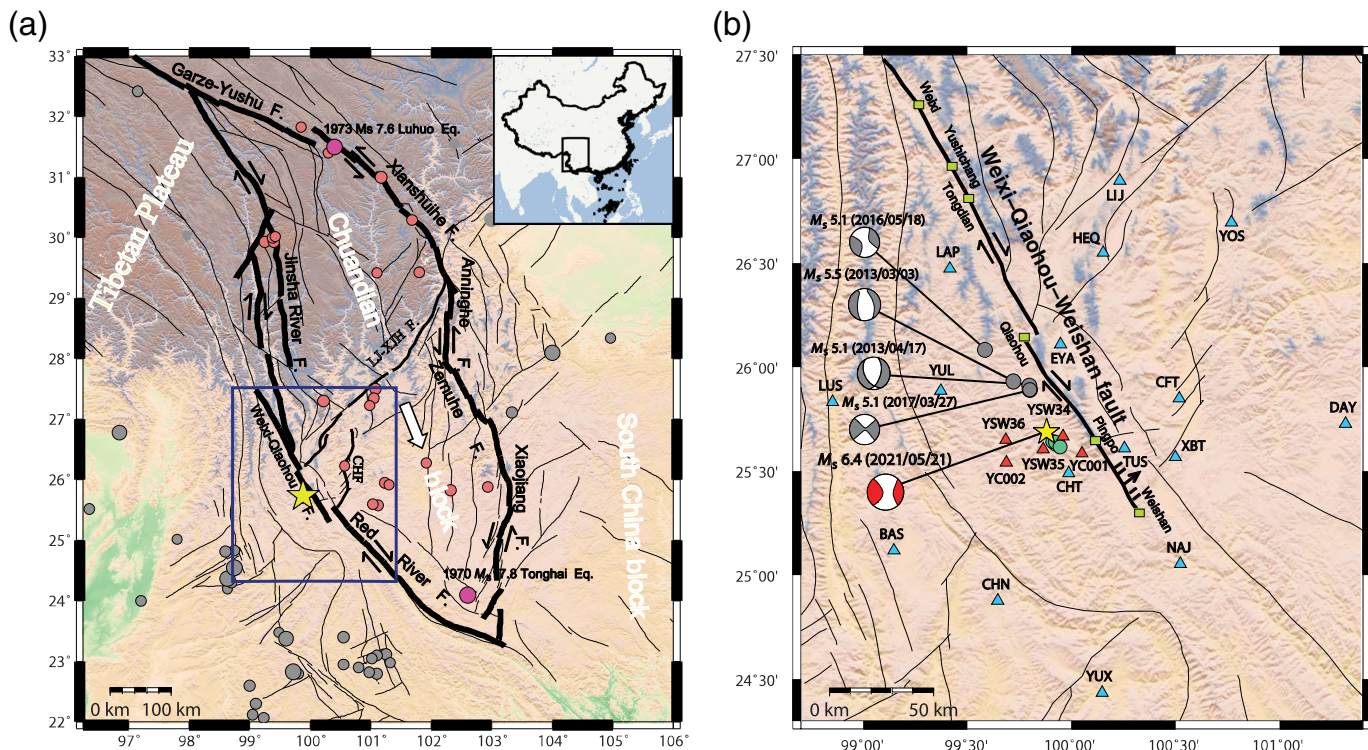
on 18 May, three days before the mainshock, with five events of magnitudes larger than 4 (Fig. 2b). The largest foreshock that has a surface-wave magnitude of 5.3 occurred at the Beijing Standard Time of 21:21 on 21 May (2021/05/21 13:21 UTC), approximately half an hour before the mainshock. This extensive foreshock sequence has contributed to mitigating the earthquake risk shortly before the mainshock. Local residents have been advised to stay in tents or outside vulnerable buildings on 20 May. Temporary seismic stations have also been installed on 20 May to monitor the sequence. Whether or not the foreshock sequence represented the nucleation process of the mainshock remains unknown. Investigating the temporal and spatial evolution of the foreshock sequence may shed light on this critical question.

Furthermore, more than 3500 aftershocks have been reported in the CENC catalog till 27 May. It is of practical significance to monitor the aftershock evolution to determine the possibility of having a relatively large magnitude quake; such a process is also critical for hazard evaluation immediately after a large earthquake. It has been shown that aftershocks may have also occurred off the ruptured fault or on a hidden conjugate fault (Ross *et al.*,

1. China Earthquake Networks Center, Beijing, China; 2. Institute of Geophysics, China Earthquake Administration, Beijing, China; 3. Sichuan Earthquake Agency, Chengdu, China; 4. Earth System Science Programme, Faculty of Science, The Chinese University of Hong Kong, Hong Kong, China, <https://orcid.org/0000-0003-4186-7375> (GZ); <https://orcid.org/0000-0002-5925-6487> (HY); 5. Yunnan Earthquake Agency, Kunming, China

\*Corresponding author: zhugaohua@link.cuhk.edu.hk

© Seismological Society of America



2019; Kato *et al.*, 2021; Yang, Liu, *et al.*, 2021). Mapping such a potential hidden source of earthquake hazard is thus valuable for emergency response and real-time hazard evaluation.

In this study, we conduct double-difference relocation of the foreshock and aftershock sequence shortly before and after the  $M_s$  6.4 mainshock, using the phase picks from the local seismic network. We also derive the focal mechanisms of relatively large foreshocks and aftershocks, as well as the distribution of  $b$ -value in the region using a long-term catalog (2008–2021). The results not only delineate the ruptured fault geometry during the mainshock but also indicate a fault that was activated during the aftershock sequence. The spatial distribution of  $b$ -value derived from background seismicity is also consistent with the occurrence of the Yangbi earthquake sequence. Furthermore, the spatiotemporal evolution of foreshocks can be well explained by cascading effects of static stress transfer.

## Tectonic Setting and Historical Earthquakes

The 2021 Yangbi earthquake sequence occurred at the southwest boundary of the Chuandian block, which is bounded by the Xianshuihe-Anninghe-Zemuhe-Xiaojiang fault system in the east and the Jinsha River–Red River fault system in the west (Fig. 1a). Because of the collision between the Indian and Eurasian plates, the Tibet Plateau was built up and part of the material escaped eastward, squeezing the Chuandian block to the southeast (Shen *et al.*, 2005). Therefore, numerous faults (e.g., Garze–Yushu fault, Xianshuihe fault, Anninghe fault, Zemuhe fault, Xiaojiang fault, etc.) along the northeast and east boundaries of the Chuandian block are left lateral, whereas those

**Figure 1.** Tectonic map and historical large earthquakes surrounding the study region. (a) The pink and fuchsia dots represent  $6.0 \leq M_s < 7.0$  and  $M_s \geq 7.0$  earthquakes, respectively. The yellow star marks the hypocenter of the  $M_s$  6.4 mainshock. Inset map shows the location of the study area with the black frame marking the region of (a). (b) The seismic stations (triangles) and historical earthquakes with focal mechanisms (gray color) and the 2021  $M_s$  6.4 earthquake sequence (green color) near the Weixi–Qiaohou–Weishan fault. The sapphire triangles are broadband permanent seismic stations of Chinese Seismic Network; the red triangles are short-period temporary stations. The color version of this figure is available only in the electronic edition.

faults (e.g., Jinsha River fault, Red River fault, and Chuxiong–Jianshui fault) along the west boundaries of the Chuandian block are mainly right-lateral strike-slip faults (Deng *et al.*, 2003). Within the block, numerous smaller scale faults have been developed, including the northeast-trending Lijiang–Xiaojinhe fault (Xiang *et al.*, 2002), the north–south-trending Chenghai fault (Yang, Duan, *et al.*, 2020), and so on.

As one of the most active blocks in China, the Chuandian block has suffered many strong earthquakes. Since 1970, there have been two earthquakes with magnitudes larger than 7 (the 1970  $M_s$  7.8 Tonghai and 1973  $M_s$  7.6 Luhuo earthquakes), and 24 earthquakes with magnitudes no less than  $M_s$  6.0. The two  $M$  7 earthquakes were both located along the block boundaries, whereas  $M$  6+ earthquakes are distributed within and along the borders of the Chuandian block (Fig. 1a).

Because the western boundary of the Chuandian block and a critical fault to accommodate the motion due to the Himalayan–

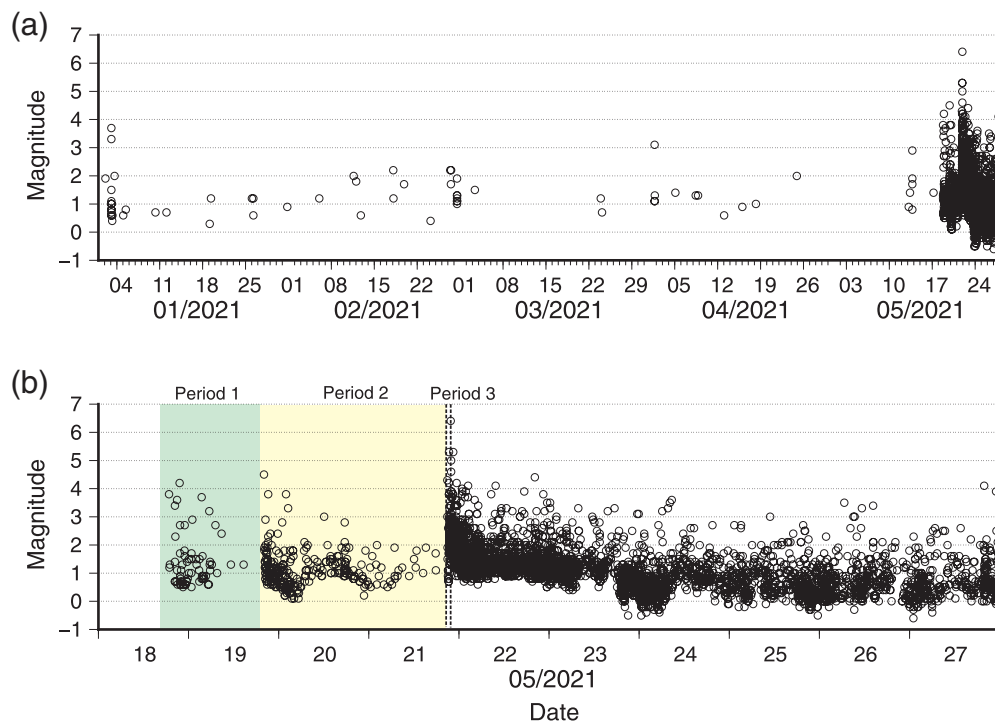


**Figure 2.** Magnitude versus time of earthquakes over the period from 1 January to 27 May 2021 (a) and period during 17–27 May 2021 (b). The three windows of period 1, 2, and 3 are colored based on the foreshock sequence appeared to be clustered temporarily. The color version of this figure is available only in the electronic edition.

Tibetan collision, the Red River fault extends more than 1000 km and has hosted numerous large earthquakes during the Pleistocene and Holocene epochs (Allen *et al.*, 1984). Historical earthquakes with magnitudes larger than  $M_s$  7.0, however, were absent along the principal segment of the Red River fault in China. The 2021 Yangbi  $M_s$  6.4 earthquake sequence directly occurred on the northwest of the Red River fault (Fig. 1a), the largest event since 1970. The closest mapped fault is the WQW fault, which is considered as induced by the northward extension of the Red River fault (Chang *et al.*, 2016). Through the field investigation, the scope and strike of the WQW fault were determined. It starts from the Baijixun area, passing through Weixi, Tongdian, Qiaohou, and ends at the southern end of the Weishan

occurred 22.5 km northwest of the 2021  $M_s$  6.4 event. Although these three earthquakes have similar focal mechanisms consistent with the property of the WQW fault, none of these historical earthquakes just fell on the fault line drawn by geologists, with an offset of approximately 15 km (Fig. 1b).

## Seismic Data

Seismic data used in this study consist of records from 16 permanent broadband seismic stations of the Chinese Seismic Network within 150 km from the earthquake sequence and five short-period stations from two temporary networks (YC and YSW) that were deployed on 20 May 2021 (Fig. 1b; Table 1). The earliest continuous record has been available since 00:24 a.m. on 20 May 2021. The five temporary stations are close to the sequence, and some epicentral distances are less than 5 km. All stations are equipped with seismometers with a sampling rate of 100 Hz. The phase picks on the temporary stations were joined to locate aftershocks at 18:06 p.m. on 23 May 2021. To get more reliable relocation results, we manually picked  $P$ - and  $S$ -wave arrivals for a total of 74 foreshocks and aftershocks with  $M_L \geq 3.0$  on the YSW stations, which are missing in the phase reports provided by the Yunnan Earthquake Agency. In addition to phase picks, we also obtain waveform data for the foreshocks and aftershocks with magnitudes larger than 4 from permanent stations, which are used to derive the focal mechanisms of foreshocks and aftershocks.

TABLE 1  
**Available Time of Temporary Stations for Phase Picking (Beijing Standard Time)**

Station Code	Available Beginning Time
YSW34	2021/05/20 00:24
YSW35	2021/05/20 15:44
YSW36	2021/05/20 12:44
YC001	2021/05/23 17:39
YC002	2021/05/23 17:38

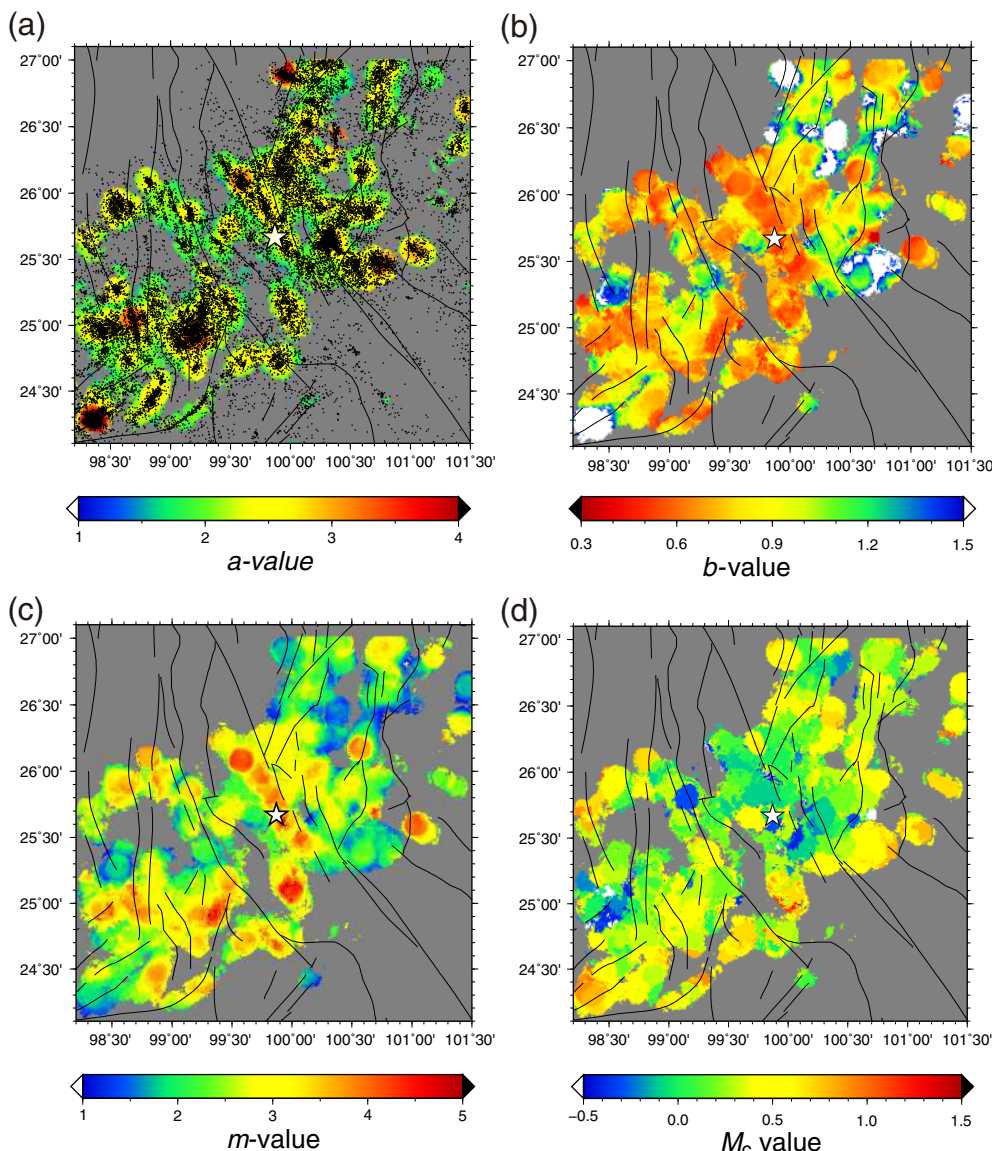


**Figure 3.** Spatial distribution of (a)  $a$ -value, (b)  $b$ -value, (c)  $M_{\max}$ , and (d)  $M_c$ -magnitude completeness in the study area based on long-term declustering catalog. The black dots in panel (a) are the earthquakes used in this analysis. The white star marks the location of the  $M_s$  6.4 Yangbi mainshock on 21 May 2021. The color version of this figure is available only in the electronic edition.

## Results

### $b$ -value

To understand the cause of frequent earthquakes in the region, we first derived the distribution of  $b$ -value using the CENC catalog from 1 October 2008 to 30 May 2021. The  $b$ -value is regarded as an indicator of regional background stress distribution (Schorlemmer *et al.*, 2005), which therefore is commonly used to evaluate earthquake risks. In fact,  $b$ -values can be significantly disturbed by a large number of aftershocks related to local stress disturbances caused by great earthquakes, making it unable to reflect the long-term background stress (Mizrahi *et al.*, 2021). Therefore, removing seismic clusters or aftershocks is necessary to calculate the  $b$ -value that may

provide predictions of the long-term occurrences of the major events.

We followed the procedures of Reasenberg (1985) to remove the earthquake clusters from October 2008 to April 2021 (Reasenberg, 1985) and selected seismic clusters in the northern section of the Red River fault zone ( $98.2^{\circ}\sim101.5^{\circ}$  E,  $24.1^{\circ}\sim27.1^{\circ}$  N). The  $b$ -value was then calculated at each grid point with an interval of  $0.01^{\circ}\times0.01^{\circ}$ . The sampling radius was set to 10 km, and the goodness-of-fit test method was used to automatically calculate the minimum magnitude completeness ( $M_c$ ) of each grid point (Wiemer and Wyss, 2000). The threshold value of the goodness-of-fit was set to 90%. For grids with at least 30 sampling events above the  $M_c$ , the maximum-likelihood method was used to calculate their  $a$ - and  $b$ -values.

In the northern section of the Red River fault zone, the  $a$ -values ranging from 2.0 to 2.5 show no obvious anomalies in the earthquake occurrence rate (Fig. 3a), but the  $b$ -values are significantly low (Fig. 3b), implying high background stress in this region. Moreover, the estimated maximum magnitudes ( $M_{\max}$ ) in the northern section of the Red River fault zone are larger

than 5 (Fig. 3c), obviously higher than those in the surrounding area, where the Yangbi  $M_s$  6.4 earthquake and 2013–2017 earthquakes (Fig. 1b) occurred. Because the declustering parameters may influence  $b$ -values (Mizrahi *et al.*, 2021), we also calculated  $b$ -values based on the catalog without declustering (Fig. S1). The results show similar patterns with the declustering results. Near the  $M_s$  6.4 mainshock region, the  $b$ -value is  $\sim 0.58$  and  $\sim 0.54$  before and after declustering, respectively.

### Earthquake location

$P$ - and  $S$ -wave arrivals were picked and visually inspected by analysts at the Yunnan Earthquake Agency. The network earthquake locations were then obtained using the LOC3D program

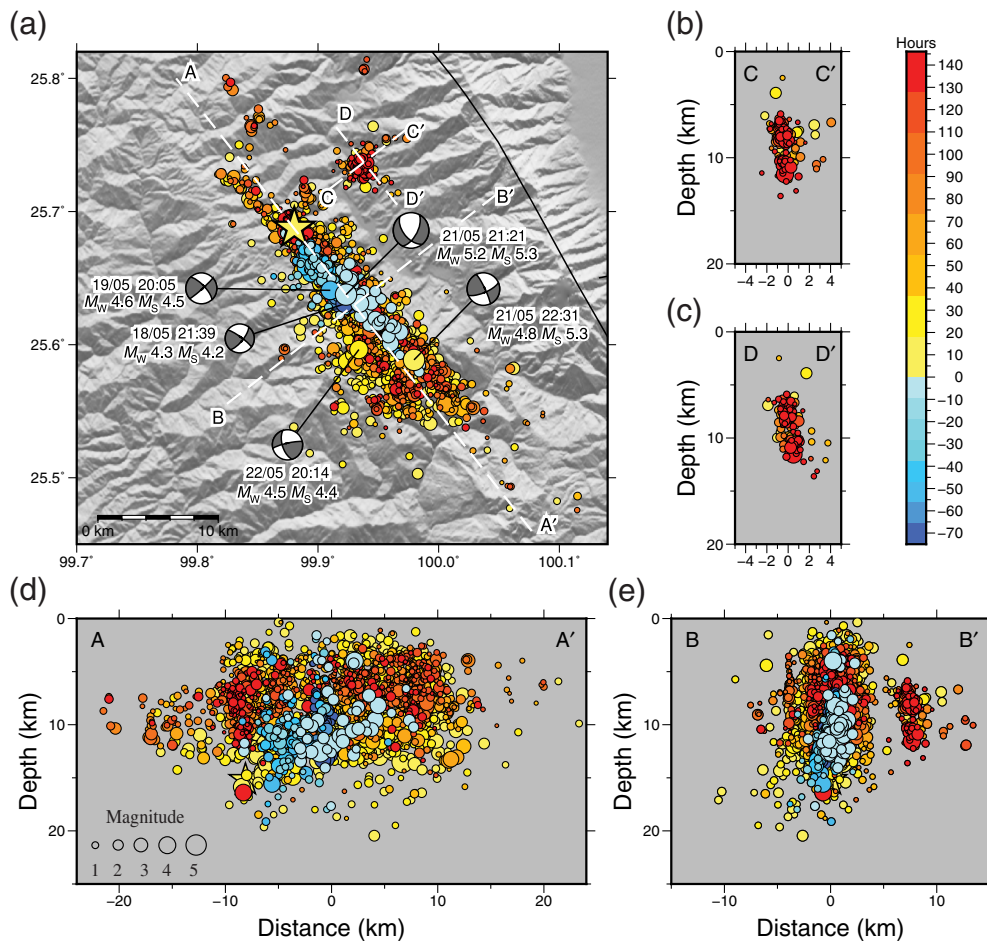


**Figure 4.** (a) Map view and (b–e) four depth profiles of relocated earthquakes over the period from 18 to 27 May 2021 and focal mechanisms of three foreshocks and two aftershocks. All the events are colored by their original time relative to the mainshock (yellow star). The circle size is scaled by the magnitude. The color version of this figure is available only in the electronic edition.

(Fang *et al.*, 2013), which was well tested in the Sichuan-Yunnan (Chuandian hereafter) region. The program calculated theoretical arrival times of regional phases using the pseudobending technique by considering topography and station elevation, based on a 3D Chuandian velocity model (Wu *et al.*, 2009) that was constructed using body-wave tomography.

The double-difference algorithm (HypoDD) (Waldbauer and Ellsworth, 2000) was employed to relocate earthquakes from 18 to 27 May. We first constructed a 1D velocity model (Fig. S2, model 3) from a surface-wave tomography model in the Chuandian region (Liu *et al.*, 2019), with shallow velocity adopted from the active source record in the nearby Binchuan basin (Yang, Duan, *et al.*, 2021b). The depth of Moho was inferred from receiver function results using a dense array in the Binchuan region (Jiang *et al.*, 2020). The ratio of  $V_p$  to  $V_s$  is set to 1.75. To ensure the location quality, we selected 2721 events with at least eight arrivals. We calculated travel-time differences for event pairs with a maximum spatial separation of 10 km, and

eventually obtained 2,958,931  $P$ -phase pairs and 2,706,990  $S$ -phase pairs. The prior weight of  $P$  and  $S$  waves were 1.0 and 0.5, respectively. A total of 2520 earthquakes, including 200 foreshocks, the mainshock, and 2319 aftershocks, were relocated (Fig. 4).

To test the reliability of the errors reported by LSQR (the conjugate gradients method) and introduced by improper station distribution, we applied the Jackknife method to estimate the variance of errors in each coordinate direction. Considering the relatively small magnitudes for most events, we used 21 stations within 150 km from the earthquake sequence. The Jackknife test repeated the location procedure 21 times, with one station removed at each run. For events that had been located more than 14 times out of the 21 runs, we then calculated their location differences in the east–west, north–south, and vertical directions relative to the mean. Finally, a total of 2520 earthquakes, including 200 foreshocks, the mainshock, and 2319 aftershocks, were relo-

cated more than 14 times during the test, and were used to estimate the standard deviation and 95% confidence interval (CI). The statistical location deviations in three directions were presented in Table S1 and Figure S3 of the supplemental material. The 95% CI shows an average location deviation of ~400 and 2000 m in horizontal and vertical directions, respectively.

The foreshocks and aftershocks during the period from 18 to 27 May 2021 span a zone with 40 and 15 km in length and width, respectively (Fig. 4a). The majority of the earthquakes are located to the southeast of the  $M_s$  6.4 mainshock epicenter, indicating a unilateral rupture of the mainshock toward the southeast. The depths of most earthquakes are shallower than 20 km, with the hypocenter of the mainshock at the depth of ~14 km. The distribution of the earthquakes delineates a nearly vertical fault plane with a slight dip angle to the southwest (Fig. 4d,e).

A large number of aftershocks following the mainshock extended to ~30 km toward the southeast along the strike, whereas some aftershocks occurred within ~10 km in the

northwest direction. The pattern of aftershocks is consistent with predominantly unilateral rupture to the southeast. Besides, a swarm of aftershocks emerged about 8 hr later in the ~10 km northeast from the mainshock, concentrated at the depth range of 5–15 km (Fig. 4b,c), indicating a nearly vertical dipping fault.

### Focal mechanisms of large foreshocks and aftershocks

To derive source parameters of the largest foreshocks and aftershocks of the 2021 Yangbi earthquake sequence, we used all available local and regional stations (Fig. S4). The double-couple solution was computed using the cut and paste (CAP) method (Zhao and Helmberger, 1994; Zhu and Helmberger, 1996). We first calculated the Green's functions using the frequency–wave-number (*f-k*) integration method (Zhu and Rivera, 2002) with different velocity models in Figure S2. For each earthquake, the seismogram was transferred to velocity (in the unit of cm/s) and the three-component seismograms were rotated to vertical, radial, and tangential components. The *Pnl* waves (vertical and radial components) and surface waves (vertical, radial, and tangential components) were filtered in the frequency band of 0.05–0.25 and 0.03–0.15 Hz, respectively. During the inversion, different segments of waveforms were allowed for separate time shifts to account for the effects of an imperfect velocity model. We then grid searched for the best source parameters ( $M_w$ , strike, dip, rake, and depth) that minimized the misfit between the observed and synthetic waveforms (Fig. 5a).

To test the robustness of our focal mechanism solutions, we performed an uncertainty analysis of the CAP inversion result using a bootstrapping inversion method. We randomly selected stations from the station pool (45 stations in total for the  $M_w$  5.2 [ $M_s$  5.3] event), with sampling 45 times and allowing repeating stations. The sampled stations (with repeating ones) were used for CAP inversion, and high weight was given for stations that were sampled multiple times. We then repeated the process 1000 times and obtained concentrated focal mechanism solutions with only a few scattered ones (Fig. 5d), suggesting a robust focal mechanism solution obtained with such a station distribution.

The  $M_w$  5.2 foreshock exhibited strike-slip faulting with the non-negligible normal-slip component, different from the other two foreshocks with nearly pure strike-slip faulting mechanism (Fig. 4a). The optimal depth of this foreshock was consistently located at depths of 6–7 km using different velocity models (Fig. 5b,c), indicating tiny effects of potential uncertainties in velocity structures. The  $M_s$  4.2 and  $M_s$  4.5 foreshocks show similar strike-slip faulting mechanisms (Fig. 4a), with one nodal plane parallel to the mapped WQW fault. We then compared their waveforms on four nearby stations following the approach in Yang, Zhou, et al. (2020). The polarities of *P* onsets were opposite at station HEQ (Fig. 6), which is located 103 km from these earthquakes. Although waveforms were largely similar in other stations, such differences suggested that the three foreshocks were originated from different faults.

### Migration of foreshocks since 18 May

We then inspected spatial and temporal pattern of the foreshocks starting from 18 May, when the foreshock sequence became intense (Fig. 2). Because the seismicity appeared to be clustered temporarily into three time windows, we conducted the analysis in three different periods, starting with the first earthquake in each period.

The first one started with an  $M_L$  3.8 foreshock that occurred ~8.1 km southeast of the  $M_s$  6.4 mainshock (Fig. 7a,d,g) on 18 May. Hereafter, we divided the mainshock ruptured fault into southeast and northwest segments, with reference to the  $M_L$  3.8 earthquake. In the following 25 hr (Fig. 7d), tens of foreshocks including one with  $M_s$  4.2 ruptured surrounding a small area northwest to the  $M_L$  3.8 foreshock, approximately 2 km in distance (Figs. 7a and 8a). This sequence lasted about 14 hr and became quiescent, except for one earthquake to the southeast (Fig. 8a). If we track the northwest migration via the seismicity front (Fig. 8a), the migration speed is estimated to be  $9.6 \pm 0.8$  km/day. The uncertainty of migration speed is estimated by considering the horizontal location deviation of ~400 m of foreshocks based on the 95% CI of the Jackknife test.

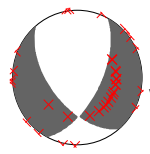
Twenty-five hours later after the  $M_L$  3.8 event, an  $M_s$  4.5 earthquake occurred near the northwest margin of the  $M_L$  3.8 sequence and was followed within 2 hr by >20 smaller magnitude earthquakes that ruptured further northwest, nearly all the way up to the  $M_s$  6.4 mainshock (Figs. 7b and 8a). The  $M_s$  4.5 foreshock sequence lasted for about 30 hr and concentrated in the northeast segment (Fig. 8a). It then stopped around 15 hr prior to the mainshock, except for a few sporadic events, including one to the southeast (Fig. 8a).

After nearly 15 hr of quiescence, an  $M_s$  4.3 foreshock occurred almost at the same location as the  $M_L$  3.8 earthquake (Figs. 7c and 8a). Less than half an hour later, an  $M_s$  5.3 event, the largest foreshock in this earthquake sequence, struck the region. Right after the  $M_s$  5.3 earthquake, seismicity in the southeast segment emerged (Figs. 7c and 8c).

## Discussion

### Foreshock sequences and implied mechanisms of nucleation

Foreshocks have been long recognized before numerous large earthquakes and are considered as one of the most effective indicators for predicting strong earthquakes, because spatiotemporal evolution of foreshocks reflects imminent stress or strength change near the source (Jones and Molnar, 1979). Experimental and theoretical studies have shown that quasi-static slip will occur before the earthquake, and the earthquake nucleation process may be accompanied by the occurrence of foreshocks (McLaskey, 2019). On a seismogenic fault with heterogeneous stress distribution, a hypocenter locating in a relatively low-stress region will result in a smaller magnitude earthquake (Yang et al., 2019), implying that the occurrence of foreshock may be an effect of where the rupture initiated. In



Event 20210521132125 Model and Depth yangbimd\_06  
FM 28 61 -41  $M_w$  5.23 rms 2.024e-01 323 ERR 1 2 3 ISO 0.00 0.00 CLVD 0.00 0.00  
Variance reduction 73.4

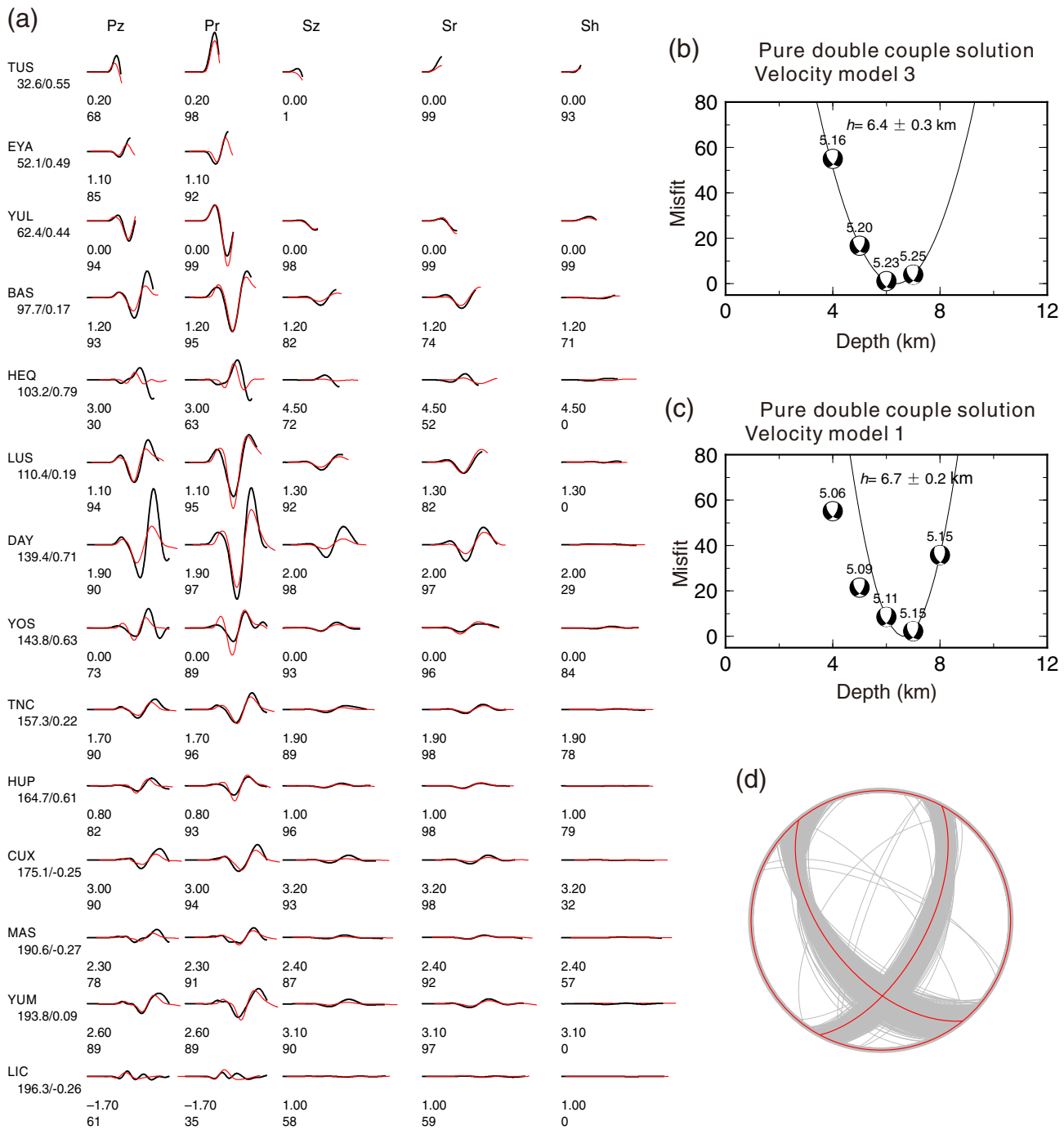


**Figure 5.** Source parameters of the  $M_w$  5.2 ( $M_s$  5.3) foreshock occurred on 21 May 2021 21:21 (2021/05/21 13:21 UTC). (a) Comparison between the observed (black lines) and best-fit synthetic (red lines) waveforms. The two numbers under each segment are the time shift in seconds (upper) between the synthetic and record (positive means a delayed record) and the waveform correlation coefficient (lower). (b, c) Waveform misfits

as a function of depth, indicating that the best depth for this event is around 6–7 km. (d) Results of bootstrapping inversion. Gray curves indicate all nodal planes of 1000 times bootstrapping inversion results, and red curves indicate the two nodal planes of the optimal solution. The color version of this figure is available only in the electronic edition.

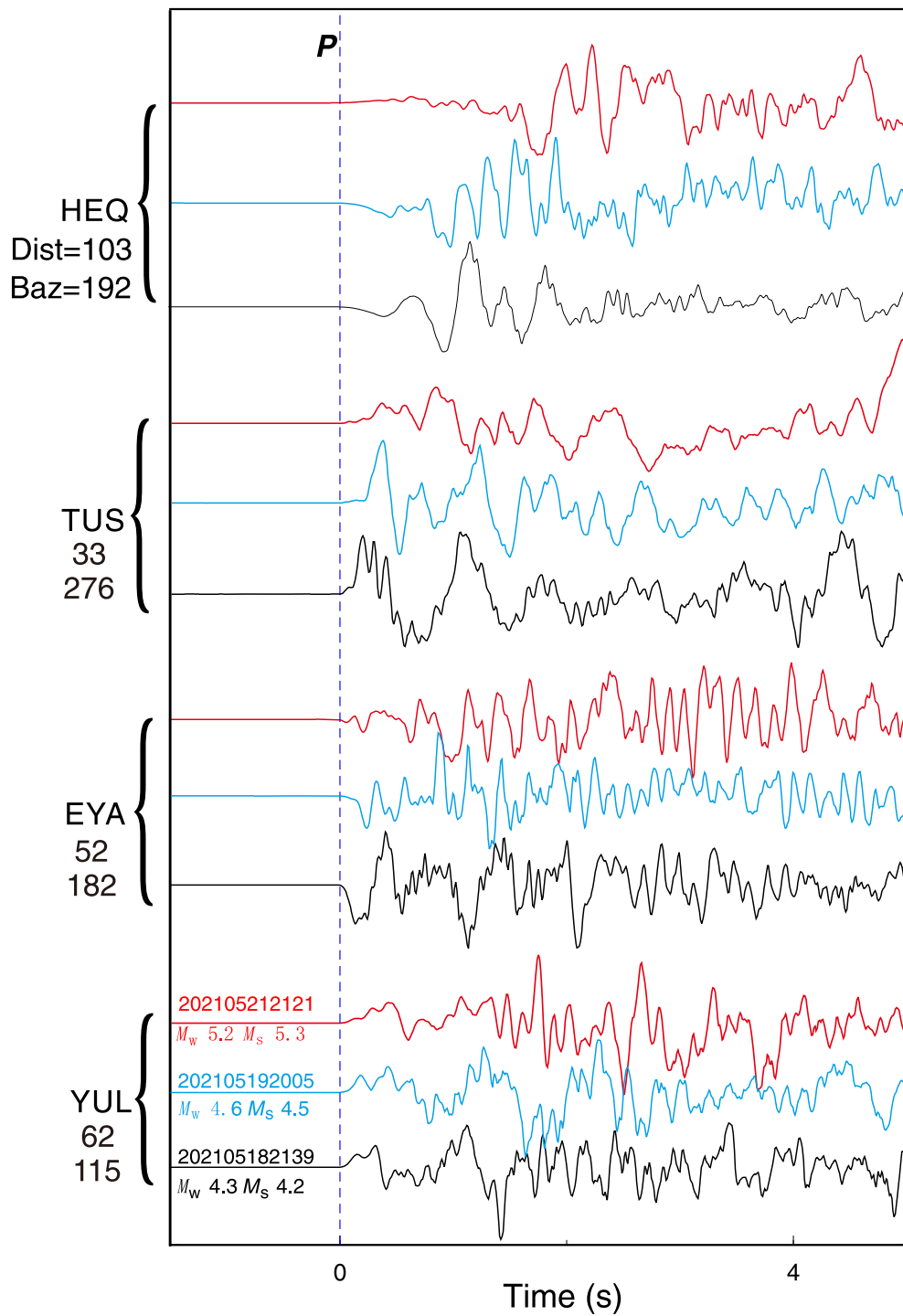


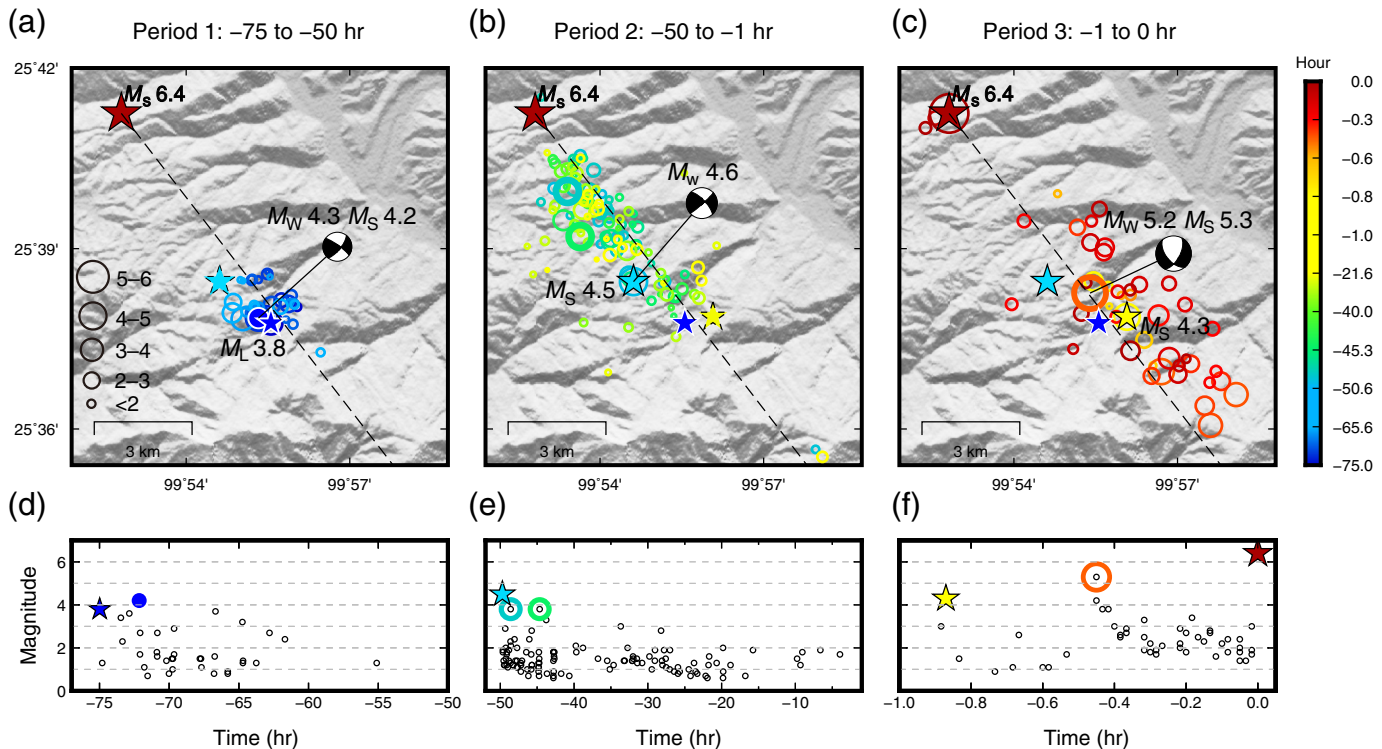
**Figure 6.** Waveform comparison of the  $M_w$  4.3 ( $M_s$  4.2),  $M_w$  4.6 ( $M_s$  4.5), and  $M_w$  5.2 ( $M_s$  5.3) foreshocks on example four stations across different distances (km) and back azimuths, shown on left. All waveforms were aligned by our manually picked  $P$ -wave arrivals. The color version of this figure is available only in the electronic edition.

contrast, spatial-temporal evolution of certain foreshock sequences has been interpreted to reflect the nucleation process of earthquakes, which is important for short-term earthquake forecasting (Kato *et al.*, 2012; Bouchon *et al.*, 2013; Ellsworth and Bulut, 2018; Huang *et al.*, 2020; Kato and Ben-Zion, 2021).

suggests a large rupture can be triggered by a mixed load of aseismic transients (pre-slip model) and the static stress transfer (cascade model) (Huang *et al.*, 2020).

Therefore, the temporal and spatial relationship of foreshocks to the hypocenter of the mainshock is critical to distinguish from

However, it remains in a debate which conceptual model, pre-slip or cascade or a combination of the two, is suitable for explaining foreshock sequences and describing earthquake nucleation processes. The pre-slip model suggests small foreshocks initiate via aseismic processes involving slow slip or fluid movement that can trigger subsequent large ruptures. This model is supported by the repeating earthquakes in foreshock sequences, migrating foreshocks (Kato *et al.*, 2012; Kato and Nakagawa, 2014), and very-low-frequency events that may transition into a large, ordinary earthquake (Tape *et al.*, 2018). In comparison, the cascade model describes that large earthquakes on a heterogeneous fault can be triggered by static and dynamic stress perturbations caused by previous neighboring earthquakes (Ellsworth and Bulut, 2018; Yoon *et al.*, 2019). One critical evidence for the cascade model is that the “repeating” foreshocks are indeed neighboring earthquakes, not true repeaters in the foreshock sequence, although their waveforms are quite similar (Ellsworth and Bulut, 2018). Besides, the cascade model can also be supported by lacking obvious precursory strain or displacement changes preceded the 2004  $M$  6.0 Parkfield earthquake based on the high-resolution continuous strain measurements (Johnston, 2006). In addition, a recent study of the foreshock sequence of the 2019 Ridgecrest  $M_w$  6.4 and  $M_w$  7.1



these mechanisms of foreshocks and understand the nucleation process of earthquakes. In this study, we did not observe consistent seismicity migration toward the mainshock. Indeed, there were only two small magnitude foreshocks ( $M_L$  2.2 and 1.9) located spatially close to the mainshock (Fig. 7b,c). All other foreshocks emerged after events with relatively large magnitudes and did not exhibit any pattern of southeast propagation from the mainshock hypocenter. Therefore, we suggested that no nucleation of the mainshock was indicated by the present results.

Moreover, there were different quiescence windows during the foreshock sequence (Fig. 8a). For instance, no foreshocks occurred on the northwest segment within the first quiescence time for  $\sim 11$  hr before the  $M_s$  4.5 earthquake (Fig. 8a). In our defined second period, within nearly 15 hr to the end of the window there were only four earthquakes in the northwest segment, having no earthquakes at least 5 hr before and after. Therefore, we called it another quiescence time (Fig. 8a). In addition, seismicity following the  $M_s$  4.5 sequence appeared to “return” to the location ruptured previously by the  $M_L$  3.8 sequence. Such quiescence windows and “back-and-forth” spatial pattern of seismicity do not favor hypotheses of a slow slip or fluid front propagating along the northwest segment (Fig. 7g).

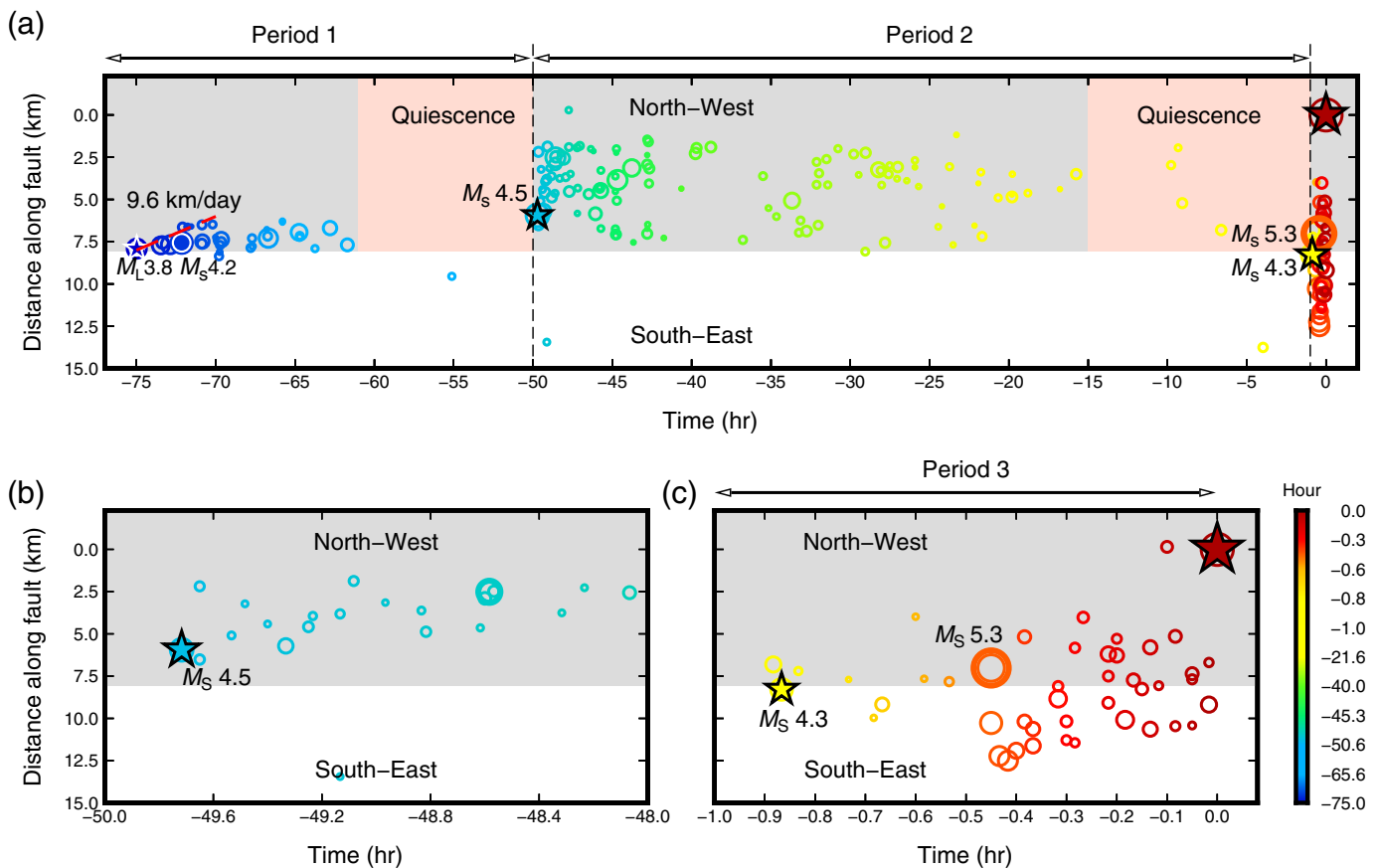
Furthermore, we did not observe concentrated or accelerated small earthquakes leading to the relatively large magnitude foreshocks either (i.e., foreshocks with  $M_L \geq 3.8$ ). Rather, the spatial and temporal pattern of all foreshocks can be well explained by static triggering (King *et al.*, 1994), particularly for those large ones occurring close to each other. Furthermore, these foreshocks may exert stress perturbation on the mainshock rupture plane, especially the largest one with  $M_s$  5.3, and thus trigger the mainshock.

**Figure 7.** Spatial-temporal evolution of the foreshock sequence colored by their original time relative to the  $M_s$  6.4 mainshock (the dark red star) in three time periods: (a) –75 to –50 hr, (b) –50 to –1 hr, and (c) –1 to 0 hr. The circle size is scaled by the magnitude. The blue, sapphire, and yellow stars mark the first event of each period. The black-dashed line represents the rupturing fault. (d–f) Magnitude versus time of foreshocks over each period. The color version of this figure is available only in the electronic edition.

Our waveform comparison of the largest foreshocks suggested that they did not occur on the identical fault, despite high similarity of their waveforms at certain stations (Fig. 6). Conducting further analysis such as rupture directivity determination (e.g., Chen *et al.*, 2021) is demanded to confirm their ruptured planes, before detailed Coulomb failure stress (CFS) can be reliably calculated. Furthermore, the diffused northwest propagation of foreshocks during period 2 may also lead to considerable stress perturbation on the fault plane ruptured during the mainshock. Calculation of shear stress changes due to these small earthquakes can be conducted after a robust mainshock rupture model is obtained.

### Off-fault aftershocks and comparison with published results

Aftershocks accompanying a mainshock are usually closely associated with the fault on which the mainshock occurs. However, the spatial distribution of aftershocks is sometimes not along the fault that ruptured during a mainshock (Marone, 2000). Laboratory experiments on fault models show that a fault system



can strongly influence its nearby stress field by fault interaction, leading to a complicated stress field even around a simple fault system, which enables off-fault earthquakes to occur on already existed tensile cracks oriented obliquely or roughly perpendicular to the main fault system (Špičák, 1988). Such kinds of off-fault aftershocks are considered to be triggered by the change in the dynamic stress or static CFS field (Das and Scholz, 1981; King *et al.*, 1994; Freed, 2005). In addition, some off-fault earthquakes are suggested to be promoted by stress changes associated with other natural forces, such as the atmospheric pressure drop caused by a hurricane (Meng *et al.*, 2018).

Although numerous aftershocks following the mainshock are consistent with the predominant rupture directivity of the mainshock, a cluster of aftershocks near the CC' profile are likely related to an activated fault. The distribution of aftershocks is generally consistent with the results reported in Jiang *et al.* (2021), Lei *et al.* (2021), Long *et al.* (2021), and Su *et al.* (2021) (all in Chinese), except that the off-fault aftershock cluster is more concentrated in our study. This off-fault cluster is located within one rupture length to the mainshock's epicenter; hence dynamic and static stress perturbations play a similarly important role. The 8 hr separation after the mainshock is not long enough to exclude the potential effects of dynamic triggering, because dynamic triggering could be time-delayed by hours to years until the evolution to failure is complete (Freed, 2005; Parsons, 2005; Shelly *et al.*, 2011). Therefore, we suggest that both dynamic and

**Figure 8.** (a–c) Space–time diagram of the foreshocks along fault strike distance. Distance is taken along the fault with 0 km corresponding to the hypocenter of the  $M_s$  6.4 mainshock. The gray shadow marks the northwest fault segment relative to the first  $M_L$  3.8 event. The colored circles and stars are corresponding to Figure 7. Red-dashed line approximate locations of the fronts of earthquake migration during period 1. The light-pink shadows mark the quiescence of foreshocks. The color version of this figure is available only in the electronic edition.

static triggering is possible for this off-fault cluster. Future CFS calculations in the near field with a precise slip model and fault parameters can help to better understand dynamics versus static triggering mechanisms for this off-fault cluster.

## Conclusions

We presented a relocated catalog of the foreshock and aftershock sequence shortly before and after the  $M_s$  6.4 mainshock using the phase picks from the local seismic network, and derived the focal mechanisms of the largest foreshocks and aftershocks as well. Waveform comparison of the largest foreshocks indicated that they were not originated from the same fault. Their close occurrence time and spatial distance were consistent with the cascade triggering hypothesis. Furthermore, the spatiotemporal evolution of foreshocks indicates neither signature of a pre-slip nucleation process of the mainshock nor slow slip and/or fluid diffusion

along the mainshock ruptured fault. Rather, they can be well explained by static stress triggering. Our present conclusions were based on the relocated earthquakes in the catalog, in which a number of low magnitude earthquakes are missing. Although the template matching method (e.g., Peng and Zhao, 2009; Yang et al., 2009) can find additional earthquakes, the “back-and-forth” spatial migration pattern of  $M_L > 3.8$  earthquakes and the lack of consistent foreshock propagation from the mainshock hypocenter will remain largely unchanged. Therefore, our preferred mechanism will still be cascading effects of static stress transfer.

Furthermore, the distribution of aftershocks suggests a predominantly unilateral rupture to the southeast, and a cluster of off-fault aftershocks indicates a nearly vertical dipping fault. Based on the statistical analysis of background seismicity during 2008–2021, the occurrence of the Yangbi earthquake sequence is well consistent with the relatively low  $b$ -value in the northern section of the Red River fault zone, which may host future damaging earthquakes.

## Data and Resources

The supplemental material includes catalogs of relocated earthquakes, table of location uncertainties, figures of uncertainty test,  $b$ -value without declustering process, and velocity models. Phase data were from China Earthquake Networks Center and Yunnan Earthquake Agency. The seismic data of temporary seismic stations are provided by Dali Center, China Seismic Experimental Site. Seismic waveform data used in this study were requested with a preauthorized account from Data Management Centre of China Seismic Network.

## Declaration of Competing Interests

The authors acknowledge that there are no conflicts of interest recorded.

## Acknowledgments

Constructive comments from two anonymous reviewers help improve this article. The authors thank Dr. Yen Joe Tan for the helpful discussion. This study is supported by the National Key R&D Program of China (2018YFC1503400), China Earthquake Science Experiment Project, China Earthquake Administration (CEA) (Grants Number 2018CSES0102), Hong Kong Research Grant Council Grants (14306418, 14303721), The Chinese University of Hong Kong (CUHK) Direct Grant from Faculty of Science, and Spark Program of Science and Technology, CEA (XH19056Y).

## References

- Allen, C. R., A. R. Gillespie, H. Yuan, K. E. Sieh, Z. Buchun, and Z. Chengnan (1984). Red River and associated faults, Yunnan province, China: Quaternary geology, slip rates, and seismic hazard, *Geol. Soc. Am. Bull.* **95**, no. 6, 686–700.
- Bouchon, M., V. Durand, D. Marsan, H. Karabulut, and J. Schmittbuhl (2013). The long precursory phase of most large interplate earthquakes, *Nat. Geosci.* **6**, 299–302.
- Chang, Z., C. Hao, Y. Zang, and B. Dai (2016). Recent active features of Weixi-Qiaohou fault and its relationship with the Honghe fault, *J. Geomech.* **22**, no. 3, 517–530.
- Chen, H., X. He, H. Yang, and J. Zhang (2021). Fault-plane determination of the 4 January 2020 offshore Pearl River delta earthquake and its implication for seismic hazard assessment, *Seismol. Res. Lett.* **92**, no. 3, 1913–1925.
- Das, S., and C. H. Scholz (1981). Off-fault aftershock clusters caused by shear stress increase? *Bull. Seismol. Soc. Am.* **71**, 1669–1675.
- Deng, Q., P. Zhang, Y. Ran, X. Yang, W. Min, and Q. Chu (2003). Basic characteristics of active tectonics of China, *Sci. China Ser. D Earth Sci.* **46**, no. 4, 356–372.
- Ekström, G., M. Nettles, and A. M. Dziewoński (2012). The global CMT project 2004–2010: Centroid-moment tensors for 13,017 earthquakes, *Phys. Earth Planet. Inter.* **200–201**, 1–9.
- Ellsworth, W. L., and F. Bulut (2018). Nucleation of the 1999 Izmit earthquake by a triggered cascade of foreshocks, *Nat. Geosci.* **11**, 531–535.
- Fang, L. H., J. P. Wu, W. L. Wang, Z. Y. Lü, C. Z. Wang, T. Yang, and Y. Cai (2013). Relocation of the mainshock and aftershock sequences of Ms 7.0 Sichuan Lushan earthquake, *Chin. Sci. Bull.* **58**, nos. 28/29, 3451–3459.
- Freed, A. M. (2005). Earthquake triggering by static, dynamic, and post-seismic stress transfer, *Annu. Rev. Earth Planet. Sci.* **33**, 335–367.
- Huang, H., L. Meng, R. Bürgmann, W. Wang, and K. Wang (2020). Spatio-temporal foreshock evolution of the 2019 M 6.4 and M 7.1 Ridgecrest, California earthquakes, *Earth Planet. Sci. Lett.* **551**, 116582.
- Jiang, J., H. Fu, and T. Li (2021). Relocation of Yangbi Ms 6.4 earthquake sequence in 2021 and discussion of its seismogenic fault, *J. Seism. Res.*, in press (in Chinese).
- Jiang, X., H. Yang, W. Yang, and W. Wang (2020). Crustal structure in the Binchuan basin of Yunnan constrained from receiver functions on a 2-D seismic dense array, *Earthq. Sci.* **33**, 264–272.
- Johnston, M. J. S. (2006). Continuous borehole strain and pore pressure in the near field of the 28 September 2004 M 6.0 Parkfield, California, earthquake: Implications for nucleation, fault response, earthquake prediction, and tremor, *Bull. Seismol. Soc. Am.* **96**, S56–S72.
- Jones, L. M., and P. Molnar (1979). Some characteristics of foreshocks and their possible relationship to earthquake prediction and premonitory slip on faults, *J. Geophys. Res.* **84**, no. B7, 3596–3608.
- Kato, A., and Y. Ben-Zion (2021). The generation of large earthquakes, *Nat. Rev. Earth and Chem.* **2**, 26–39.
- Kato, A., and S. Nakagawa (2014). Multiple slow-slip events during a foreshock sequence of the 2014 Iquique, Chile Mw 8.1 earthquake, *Geophys. Res. Lett.* **41**, 5420–5427.
- Kato, A., K. Obara, T. Igarashi, H. Tsuruoka, S. Nakagawa, and N. Hirata (2012). Propagation of slow slip leading up to the 2011 Mw 9.0 Tohoku-Oki earthquake, *Science* **335**, 705–708.
- Kato, A., S. I. Sakai, S. Matsumoto, and Y. Iio (2021). Conjugate faulting and structural complexity on the young fault system associated with the 2000 Tottori earthquake, *Commun. Earth Environ.* **2**, no. 1, 13.
- King, G. C. P., R. S. Stein, and J. Lin (1994). Static stress changes and the triggering of earthquakes, *Bull. Seismol. Soc. Am.* **84**, 935–953.
- Lei, X., Z. Wang, S. Wang, and C. He (2021). A preliminary study on the characteristics and mechanism of the May 2021 MS6.4, Yangbi earthquake sequence, Yunnan, China, *Acta Seismol. Sin.* **43**, no. 3, 261–286, doi: [10.11939/jass.20210100](https://doi.org/10.11939/jass.20210100) (in Chinese).
- Liu, C., H. Yao, H.-Y. Yang, W. Shen, H. Fang, S. Hu, and L. Qiao (2019). Direct inversion for three-dimensional shear wave speed azimuthal anisotropy based on surface wave ray tracing: Methodology

- and application to Yunnan, southwest China, *J. Geophys. Res.* **124**, 11,394–11,413.
- Long, F., Y. Qi, G. Yi, W. Wu, G. Wang, X. Zhao, and G. Peng (2021). Relocation of the Ms 6.4 Yangbi earthquake sequence on May 21, 2021 in Yunnan province and its seismogenic structure analysis, *Chin. J. Geophys.* **64**, no. 8, 2631–2646, doi: [10.6038/cjg2021O0526](https://doi.org/10.6038/cjg2021O0526) (in Chinese).
- Marone, C. (2000). Shaking faults loose, *Nature* **408**, 533–535.
- McLaskey, G. C. (2019). Earthquake initiation from laboratory observations and implications for foreshocks, *J. Geophys. Res.* **124**, 12,882–12,904.
- Meng, X., H. Yang, and Z. Peng, (2018). Foreshocks, b value map, and aftershock triggering for the 2011 Mw 5.7 Virginia earthquake, *J. Geophys. Res.* **123**, 5082–5098.
- Mizrahi, L., S. Nandan, and S. Wiemer (2021). The effect of declustering on the size distribution of mainshocks, *Seismol. Res. Lett.* **92**, no. 4, 2333–2342.
- Parsons, T. (2005). A hypothesis for delayed dynamic earthquake triggering, *Geophys. Res. Lett.* **32**, L04302.
- Peng, Z., and P. Zhao (2009). Migration of early aftershocks following the 2004 Parkfield earthquake, *Nat. Geosci.* **2**, no. 12, 877–881.
- Reasenberg, P. (1985). Second-order moment of central California seismicity, 1969–1982, *J. Geophys. Res.* **90**, 5479–5495.
- Ross, Z. E., B. Idini, Z. Jia, O. L. Stephenson, M. Zhong, X. Wang, Z. Zhan, M. Simons, E. J. Fielding, S. H. Yun, et al. (2019). Hierarchical interlocked orthogonal faulting in the 2019 Ridgecrest earthquake sequence, *Science* **366**, no. 6463, 346–351.
- Schorlemmer, D., S. Wiemer, and M. Wyss (2005). Variations in earthquake-size distribution across different stress regimes, *Nature* **437**, 539.
- Shelly, D. R., Z. Peng, D. P. Hill, and C. Aiken (2011). Triggered creep as a possible mechanism for delayed dynamic triggering of tremor and earthquakes, *Nat. Geosci.* **4**, 384–388.
- Shen, Z. K., J. Lü, M. Wang, and R. Bürgmann (2005). Contemporary crustal deformation around the southeast borderland of the Tibetan Plateau, *J. Geophys. Res.* **110**, B11409.
- Špičák, A. (1988). Laboratory investigation into off-fault seismic activity, *Bull. Seismol. Soc. Am.* **78**, 1232–1242.
- Su, J., M. Liu, Y. Zhang, W. Wang, H. Li, J. Yang, X. Li, and M. Zhang (2021). High resolution earthquake catalog building for the 21 May 2021 Yangbi, Yunnan, MS6.4 earthquake sequence using deep-learning phase picker. *Chin. J. Geophys.* **64**, no. 8, 2647–2656, doi: [10.6038/cjg2021O0530](https://doi.org/10.6038/cjg2021O0530) (in Chinese).
- Tape, C., S. Holtkamp, V. Silwal, J. Hawthorne, Y. Kaneko, J. P. Ampuero, C. Ji, N. Ruppert, K. Smith, and M. E. West (2018). Earthquake nucleation and fault slip complexity in the lower crust of central Alaska, *Nat. Geosci.* **11**, 536–541.
- Waldhauser, F., and W. L. Ellsworth (2000). A double-difference earthquake location algorithm: Method and application to the northern Hayward fault, California, *Bull. Seismol. Soc. Am.* **90**, 1353–1368.
- Wang, Q., R. Chu, H. Yang, L. Zhu, and Y. Su (2018). Complex rupture of the 2014 Ms 6.6 Jinggu earthquake sequence in Yunnan province inferred from double-difference relocation, *Pure Appl. Geophys.* **175**, 4253–4274.
- Wiemer, S., and M. Wyss (2000). Minimum magnitude of completeness in earthquake catalogs: Examples from Alaska, the western United States, and Japan, *Bull. Seismol. Soc. Am.* **90**, 859–869.
- Wu, J. P., Y. Huang, T. Z. Zhang, Y. H. Ming, and L. H. Fang (2009). Aftershock distribution of the Ms 8.0 Wenchuan earthquake and three dimensional P-wave velocity structure in and around source region, *Acta Geophys. Sin.* **52**, no. 2, 320–328, doi: [10.1002/cjg2.1331](https://doi.org/10.1002/cjg2.1331).
- Xiang, H. F., X. W. Xu, S. M. Guo, W. X. Zhang, H. W. Li, and G. H. Yu (2002). Sinistral thrusting along the Lijiang-Xiaojinhe fault since the quaternary and its geologic-tectonic significance - Shielding effect of transverse structure of intracontinental active block, *Seismol. Geol. (in Chinese)* **24**, no. 2, 188–198.
- Yang, H., Y. Duan, J. Song, X. Jiang, X. Tian, W. Yang, W. Wang, and J. Yang (2020). Fine structure of the Chenghai fault zone, Yunnan, China, constrained from teleseismic travel time and ambient noise tomography, *J. Geophys. Res.* **125**, no. 7, 1–14.
- Yang, H., Y. Duan, J. Song, W. Yang, W. Wang, X. Tian, and B. Wang (2021). Illuminating high-resolution crustal fault zones and temporal changes using multi-scale dense arrays and airgun sources, *Earthq. Res. Adv.*, doi: [10.19743/j.cnki.0891-4176.202101002](https://doi.org/10.19743/j.cnki.0891-4176.202101002).
- Yang, H., S. Yao, B. He, and A. V. Newman (2019). Earthquake rupture dependence on hypocentral location along the Nicoya Peninsula subduction megathrust, *Earth Planet. Sci. Lett.* **520**, 10–17.
- Yang, H., P. Zhou, N. Fang, G. Zhu, W. Xu, J. Su, F. Meng, and R. Chu (2020). A shallow shock: The 25 February 2019 ML 4.9 earthquake in the weiyuan shale gas field in Sichuan, China, *Seismol. Res. Lett.* **91**, 3182–3194.
- Yang, H., L. Zhu, and R. Chu (2009). Fault-plane determination of the 18 April 2008 Mount Carmel, Illinois, earthquake by detecting and relocating aftershocks, *Bull. Seismol. Soc. Am.* **99**, no. 6, 3413–3420.
- Yang, J., Y. Su, X. Li, B. Ye, and J. Chen (2015). Research on focal mechanism solutions of  $ML \geq 3.4$  earthquakes of Eryuan Ms 5.5 earthquake sequence in 2013, *J. Seismol. Res.* **38**, no. 2, 196–202.
- Yang, Z., J. Liu, X. Zhang, W. Deng, G. Du, and X. Wu (2021). A preliminary report of the Yangbi, Yunnan, Ms 6.4 earthquake of May 21, 2021, *Earth Planet. Phys.* **5**, no. 4, 1–3.
- Yoon, C. E., N. Yoshimitsu, W. L. Ellsworth, and G. C. Beroza (2019). Foreshocks and mainshock nucleation of the 1999 Mw 7.1 Hector Mine, California, earthquake, *J. Geophys. Res.* **124**, 1569–1582.
- Zhang, K., W. Gan, S. Liang, G. Xiao, C. Dai, Y. Wang, Z. Li, L. Zhang, and G. Ma (2021). Coseismic displacement and slip distribution of the 2021 May 21, MS 6.4, Yangbi Earthquake derived from GNSS observations. *Chin. J. Geophys.* **64**, no. 7, 2253–2266, doi: [10.6038/cjg2021O0524](https://doi.org/10.6038/cjg2021O0524) (in Chinese).
- Zhao, L.-S., and D. V. Helmberger (1994). Source estimation from broadband regional seismograms, *Bull. Seismol. Soc. Am.* **84**, 91–104.
- Zhu, L., and D. V. Helmberger (1996). Advancement in source estimation techniques using broadband regional seismograms, *Bull. Seismol. Soc. Am.* **86**, 1634–1641.
- Zhu, L., and L. A. Rivera (2002). A note on the dynamic and static displacements from a point source in multilayered media, *Geophys. J. Int.* **148**, 619–627.

Manuscript received 17 June 2021  
Published online 3 November 2021